CRYSTAL GROWTH & DESIGN

pubs.acs.org/crystal

Article

Exploration of Vanadium(IV)-Based Single-Ion Magnet Properties in Diphosphonate-Supported Mixed-Valent Polyoxovanadates

Published as part of a Crystal Growth and Design virtual special issue on Molecular Magnets and Switchable Magnetic Materials

Pragyansh Singh, Sören Schlittenhardt, Dewendra Thakre, Saroj Kumar Kushvaha, Sunil Kumar, Harsha S. Karnamkkott, Mario Ruben, Masooma Ibrahim, Abhishek Banerjee,* and Kartik Chandra Mondal*

Cite This: *Cryst. Growth Des.* 2022, 22, 5666−5679

Read Online

ACCESS | Metrics & More | Article Recommendations | Supporting Information

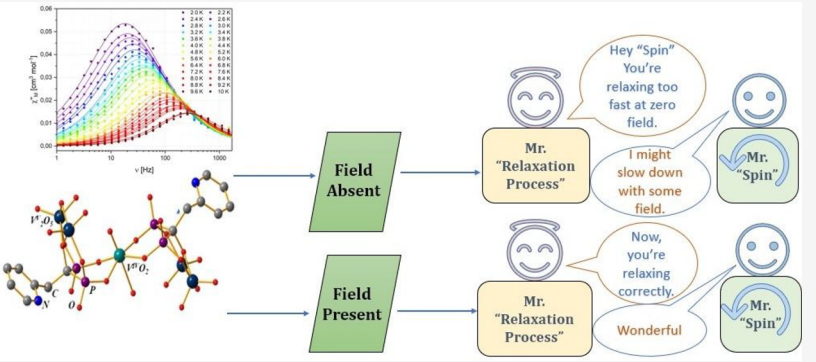

ABSTRACT: Due to their potential future applications in high-density data storage devices, single-ion magnets (SIMs) have become one of the most exciting classes of materials for research at present. Vanadium complexes, with their unique multiple oxidation states and coordination geometries, are excellent candidates for investigating such properties. In the present study, we have explored the SIM properties of two mixed-valent organo-polyoxovanadyl complexes, viz. $(NH_4)_4[H_6(V^{IV}O_2)(V^{V}{}_2O_5)_2\{O_3P\text{-}C(O)(CH_2\text{-}2\text{-}C_5NH_4)\text{-}PO_3\}_2]\cdot 9H_2O$ (**1**) and $(NH_4)_4[H_6(V^{IV}O_2)(V^{V}{}_2O_5)_2\{O_3P\text{-}C(O)(CH_2\text{-}3\text{-}C_5NH_4)\text{-}PO_3\}_2]\cdot 8H_2O$ (**2**), each of which contains four vanadium(V) atoms and one vanadium(IV) atom. One unpaired electron on the central Kramers vanadium(IV) ($S = 1/2$) atom gives the molecule its magnetic moment, which is responsible for the reversal of its magnetization/spin at low temperatures. As such, the investigation of these complexes has involved a combination of experimental techniques, including superconducting quantum interference device (SQUID) magnetometry, electron paramagnetic resonance (EPR) spectroscopy, and a computational technique that used the CASSCF-based wave function theory and included relativistic effects by considering NEVPT2 for more accurate results. AC magnetic susceptibility measurements have revealed the single ion magnet (SIM) behaviors of both the complexes under the application of an external DC magnetic field, which were characterized by maxima in the plots of the "out-of-phase" magnetic susceptibility against the AC frequency (χ'' *vs* ν) at different temperatures. The spin relaxation time (τ) has been determined to be in the range of 2−10 K. From the fitting of the plot of relaxation time (τ) versus temperature to different models, we have tried to understand the type of slow relaxation process present in the system under a particular applied DC magnetic field. Finally, the *ab initio* method, viz. the CASSCF-based computational methods, has been employed to justify/rationalize and correlate the experimental results.

1. INTRODUCTION

Single-molecule magnets (SMMs), which are characterized by their ability to display slow relaxation of magnetization and magnetic hysteresis loop, have attracted massive research interest over the past three decades.[1] The significance of SMMs lies in their potential applications in nanomagnetism,[2] spintronics,[3] and quantum information processing.[4−7] The robustness of the SMMs is measured in terms of their chemical

Received: July 4, 2022
Revised: August 4, 2022
Published: August 22, 2022

stability, desired magnetization dynamics, and ability to be deposited on surfaces or filled in nanogaps.[8] However, the primary impediment toward the greater application of such materials is that their SMM behavior manifests only at temperatures significantly lower than room temperature. Therefore, efforts in this field have been primarily focused on increasing the operating temperatures of SMMs to liquid nitrogen temperature or preferably room temperature. The performance of SMMs is typically defined by two parameters: the effective energy barrier to slow relaxation of magnetization, U_{eff}, and the magnetic blocking temperature, T_B.[9] While these two variables are linked, only T_B directly reflects the performance of the SMM material for practical use. The so-called magnetic blocking temperature T_B is thus defined as the temperature below which the relaxation of the magnetization becomes slow compared to the time scale of the particular investigation technique. Therefore, considerable efforts toward increasing the T_B of such materials are currently underway.

SMMs that contain a single paramagnetic center responsible for slow relaxation of their magnetizations are called single-ion magnets (SIMs). In particular, lanthanide-based SIMs have emerged as one of the most successful classes of SIMs in terms of the energy barrier for relaxation of magnetization (U_{eff}) and the blocking temperature (T_B). Therefore, they are considered to be the most suitable candidates for nanomagnet applications, which can take advantage of the favorable unquenched angular orbital momentum.[10−12] Looking at the most recent examples of SMMs, a dilanthanide complex containing a metal−metal bond, reported by Long et al. in 2022, has an energy barrier and a blocking temperature of 1631 cm^{-1} and 72 K, respectively.[13] A dysprosium metallocene-based SIM, reported in 2018, for which the magnetic hysteresis has been achieved at liquid nitrogen temperature afforded an effective energy barrier of U_{eff} = 1543 cm^{-1}.[10] Although magnetic hysteresis at liquid nitrogen temperature is a record improvement in the blocking temperature, room-temperature hysteresis in SMMs has yet to be realized, which limits their practical usability in high-density data storage devices. To overcome these limitations, chemists have been putting in continuous efforts by employing different strategies such as tuning the anisotropy and geometry of the complexes, which requires the careful selection of metal ion and ligand systems when undertaking the synthesis.[14,15] The key point in these synthetic approaches involves minimizing the quantum tunnelling of magnetization (QTM) so that the effective energy barrier can be raised, since the QTM regime greatly weakens the performance of SMMs and sometimes causes slow relaxation to disappear at zero applied field. In such cases, the application of an external DC field may result in the observance of slow spin or relaxation of magnetization.[16]

While the phenomenon of QTM in SMMs is considered a problem for data storage applications, because it leads to the loss of information, it is an essential prerequisite for the read-out and manipulation of nuclear states in quantum information processing schemes.[17] Therefore, the process of QTM has the potential to realize quantum computers, which are being pursued due to their unparalleled computing capabilities, wherein the electronic and nuclear spins can be used as quantum bits (qubits) within the lifetime of quantum superposition.

The unpaired electronic spins present in certain coordination complexes are inherently quantum objects containing two states, $M_S = \pm 1/2$; therefore, they can be put into quantum superposition states through the use of pulsed microwaves.[18] Since coordination complexes are highly tunable, the molecular qubits can be chemically coupled to give functional devices.[19] Particularly, vanadium(IV)-based SMMs are potential nuclear spin systems for qubits, due to their ability to afford longer coherence times.[20] Literature reports suggest that vanadium(IV) complexes containing spin-free ligand systems can exhibit coherence times at low temperatures, that are long enough to perform quantum operations.[6,21−23] Similarly, SIMs based on vanadium(III) have also been reported to display interesting magnetization dynamics.[24−26]

Keeping in mind such interesting magnetic properties of vanadium(IV)-based SMMs, we explored the SIM properties of two mixed-valent organo-polyoxovanadate(IV/V) complexes, viz. $(NH_4)_4[H_6(V^{IV}O_2)(V^{V}_2O_5)_2\{O_3P\text{-}C(O)(CH_2\text{-}2\text{-}C_5NH_4)\text{-}PO_3\}_2]\cdot 9H_2O$ (**1**), and $(NH_4)_4[H_6(V^{IV}O_2)\text{-}(V^{V}_2O_5)_2\{O_3P\text{-}C(O)(CH_2\text{-}3\text{-}C_5NH_4)\text{-}PO_3\}_2]\cdot 8H_2O$ (**2**). Such a mixed-valent assembly is essentially stabilized by the supporting organic diphosphonate ligand(s). The investigation of the dynamics of magnetization revealed that the complexes only display slow relaxation of magnetization when an external DC magnetic field is applied.

2. RESULTS AND DISCUSSION

2.1. Structural Description. The overall structures of the complexes, $(NH_4)_4[H_6(V^{IV}O_2)(V^{V}_2O_5)_2\{O_3P\text{-}C(O)(CH_2\text{-}2\text{-}C_5NH_4)\text{-}PO_3\}_2]\cdot 9H_2O$ (**1**) and $(NH_4)_4[H_6(V^{IV}O_2)\text{-}(V^{V}_2O_5)_2\{O_3P\text{-}C(O)(CH_2\text{-}3\text{-}C_5NH_4)\text{-}PO_3\}_2]\cdot 8H_2O$ (**2**), were determined by single-crystal X-ray diffraction.[27,28] Both the complexes were found to be isostructural with each other and crystallized in the same noncentrosymmetric orthorhombic space group of $P2_12_12$, with the only difference being in the locations of the counterions and cocrystallized solvent water molecules.

The structures of complexes **1** and **2** have been previously reported in the literature.[27] The asymmetric unit of the polyanionic moieties in both complexes **1** and **2** consists of 51 non-hydrogen atoms comprising 5 vanadium, 4 phosphorus, 26 oxygen, 2 nitrogen, and 14 carbon atoms. As mentioned earlier, the polyanionic complexes **1** and **2** are observed to be mixed-valent in nature. Of the total five vanadium atoms present in each polyanionic complex, V(1) is in the +4 oxidation state and V(2)−(5) are in the +5 oxidation state, as determined by bond-valence sum calculations (see Supporting Information Tables S2 and S3). Furthermore, the coordination environments of the different valent vanadium atoms were also observed to be dissimilar, with the vanadium(IV) atom adopting a six-coordinate distorted octahedral geometry and the vanadium(V) atoms adopting a five-coordinate square pyramidal geometry. The structures of the polyanionic complexes **1** and **2** are thus composed of two dimeric $\{V^{V}_2O_5\}$ units and a single octahedral $\{V^{IV}O_6\}$ unit, which are connected alternatively via the two diphosphonate ligands at opposite sides. The diphosphonate units are connected via both P−O−V and C−O−V linkages and are oriented in opposite directions, leading to the overall structures that resemble an S-shape and have an idealized point-group symmetry of C_{2v} for both polyanionic structures (see Figure 1a and 1b for polyanion complexes **1** and **2**, respectively). Ostensibly, due to the presence of the diphosphonate ligand(s), which connect the different-oxidation-state vanadium atoms with varying coordination environments within the same polyanionic complex (five- and six-coordinate for

https://doi.org/10.1021/acs.cgd.2c00754
Cryst. Growth Des. 2022, 22, 5666−5679

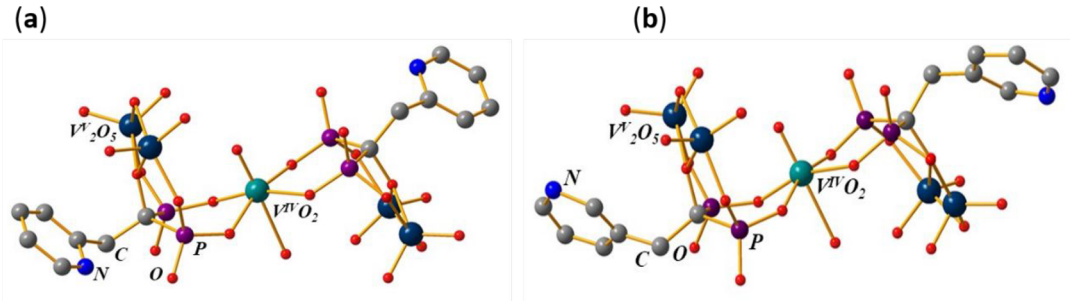

Figure 1. Ball-and-stick representation of (a) polyanion complex $[(V^{IV}O_2)(V^{V}_2O_5)_2\{O_3P\text{-}C(O)(CH_2\text{-}2\text{-}C_5NH_4)\text{-}PO_3\}_2]^{10-}$ (**1**) and (b) polyanion complex $[(V^{IV}O_2)(V^{V}_2O_5)_2\{O_3P\text{-}C(O)(CH_2\text{-}3\text{-}C_5NH_4)\text{-}PO_3\}_2]^{10-}$ (**2**). The color code is as follows: vanadium(V), teal; vanadium(IV), green; phosphorus, magenta; oxygen, red; nitrogen, blue; and carbon, gray. Hydrogen atoms on carbon have been omitted for clarity. Adapted from ref 27. Copyright 2021 American Chemical Society. Also adapted from ref 28. Copyright 2021 Elsevier.

V(V) and V(IV), respectively), the polyoxovanadates **1** and **2** are some of the few examples of stable mixed-valent oxo-vanadate complexes reported thus far.[21,22,29,30]

For complex **1**, the vanadium−oxygen bond distances for V(V) atoms are in the range of 1.59−2.041 Å, with an average bond length of 1.837 Å, while the vanadium−oxygen bond distance for the V(IV) atoms are in the range of 1.583−2.363 Å, with an average bond distance of 1.983 Å (see Supporting Information Table S4). Similarly, for complex **2**, the vanadium−oxygen bond distances corresponding to V(V) atoms are in the range of 1.54−2.03 Å, with an average bond length of 1.833 Å, while the vanadium−oxygen bond distances corresponding to V(IV) atom are in the range of 1.57−2.38 Å, with an average bond distance of 1.983 Å (see Supporting Information Table S5). The vanadium−oxygen bond distances are typical of other oxo-vanadate complexes.[31−33] Interestingly, both extremely short and an extremely long vanadium−oxygen bonds for the vanadium(IV) atom were observed in these structures, with bond-distances of 1.58 and 1.57 Å for the short bond(s) and 2.363 and 2.38 Å for the long bond(s) for complexes **1** and **2**, respectively. These bonds lead to a significantly Jahn−Teller distorted octahedral environment for the vanadium(IV) atom(s). For the centrally located vanadium(IV) atom, the bond angle between the axial ligands, which are trans to each other, is 177.2°, whereas those for the similar trans ligands present on the equatorial plane are 159.4° and 160.9°, respectively. This suggests the development of possible significant anisotropy around this centrally located vanadium(IV) atom (see Supporting Information Tables S6 and S7 for **1** and **2**, respectively). Given the extreme short and long opposite vanadium(IV)−oxygen bond(s), the vanadium-(IV) atom can thus be ascertained to form a double bond with the proximal oxygen, and the distal oxygen atom can be ascertained to be a water ligand. This was further confirmed by the elemental analysis data, which showed the presence of extra hydrogen atoms in the formula. As such, there are very few examples of such vanadium-oxo−water complexes in the literature.[34] The S-shaped structures of complexes **1** and **2** have also been reported with other diphosphonate ligands, as for example, the polyanion $[(V_5O_9(OH)_2(H_2O)\{O_3P\text{-}C(O)\text{-}(C_3H_6NH_3)\text{-}PO_3\}_2]^{4-}$ with 1-hydroxy-2-(imidazole-1-yl)-ethane-1,1-diphosphonic acid, reported by Mialane and co-workers.[30] In this structure, similar short and long vanadium−oxygen bonds for the central vanadium(IV) atom were observed (bond distances of 1.575 and 2.348 Å, respectively).[30] However, unlike complexes **1** and **2**, in this structure the authors assigned one of the oxygens bonded to the central vanadium(IV) as a hydroxo ligand and another as a water ligand.

The complexes **1** and **2** are obviously not ideally shaped. Therefore, to further describe the structural distortion in the coordination geometry of complex **1**, we quantified the distortion with continuous shape measures (CShM), as described by Avnir et al.[35,36] The complex was investigated for distortion with respect to ideal octahedron $\mathbf{S}(O_h)$ and trigonal prism $\mathbf{S}(D_{3h})$ geometries. The values obtained from the analysis provide an estimation of deviation from the respective geometry, where 0 represents the ideal geometry. The CShM data (see Table 1) show that the complex is closest to an ideal octahedron with a value of 0.524, whereas trigonal prismatic (TPR) geometry was estimated to have a value of 15.773, indicating that the complex is definitely not closer to being TPR.

Table 1. Computed CShM Parameters for Complex 1

considered geometry	*S*
octahedron (OC-6)	0.524
trigonal prism (TPR-6)	15.773

2.1.1. AILFT and Natural Bonding Orbital (NBO) Structural Analysis. The AILFT and NBO computational studies are fundamentally different from each other and were employed with the help of two different theories, viz. ab initio and DFT, respectively. The AILFT approach essentially focuses on the effect of the ligand field environment at the energy levels of the metal and is hence very helpful for mapping the electronic behavior. Subsequently, one is able to extract the LFT parameters, including the one electron matrix, Racah parameters, and the spin−orbit coupling parameter (ζ).[37,38] Meanwhile, the NBO approach is based on the mixing of orbitals and predicts the atoms involved in the interaction. Therefore, AILFT will take precedence for tracing the electron presence in metal orbitals, whereas NBO analysis will take precedence for taking into account various bonding properties and their populations.

The geometry optimization of complex **1** suggests that the central vanadium(IV) atom is coordinated by four equatorial oxygen atoms (V^{IV}−O bond distances of 1.972−2.018 Å), which agrees with the structurally characterized distance of 1.984−1.995 Å.[39,40] The calculated V(IV)═O bond distance toward the axially coordinated oxygen is 1.611 Å, which is slightly higher than the corresponding experimental distance of 1.582 Å.[41−43] The optimization resulted in the dissociation of

https://doi.org/10.1021/acs.cgd.2c00754
Cryst. Growth Des. 2022, 22, 5666−5679

the coordinated water molecule, suggesting a weak bond interaction between the solvent molecule and the respective metal center. This in turn results in a minorly distorted square pyramidal coordination geometry, which was verified by once again making use of CShM (see Supporting Information S13), instead of the characterized distorted octahedral coordination geometry for the central vanadium(IV) atom present within the polyanion complex, as derived from the crystal information file.

The structural deviation of the molecule from the ideal geometry will also distort the energy levels. To better understand the ligand−metal interactions, the orbital energy levels of the ideal square pyramidal geometry and dominating ground-state configuration computed with AILFT module in the CASSCF + NEVPT2 calculation were compared (see Figure 2). For better reference, the ligand field was considered to be a one-electron eigenfunction table (see Table S8 in Supporting Information Table S8). Observing the table, it is pretty evident that the ground state is dominated with the configuration having the single electron in the orbital "$d_{x^2-y^2}$". Another noticeable point is that the orbital energies are mentioned in the relative reference with the ground-state orbital (0 eV).

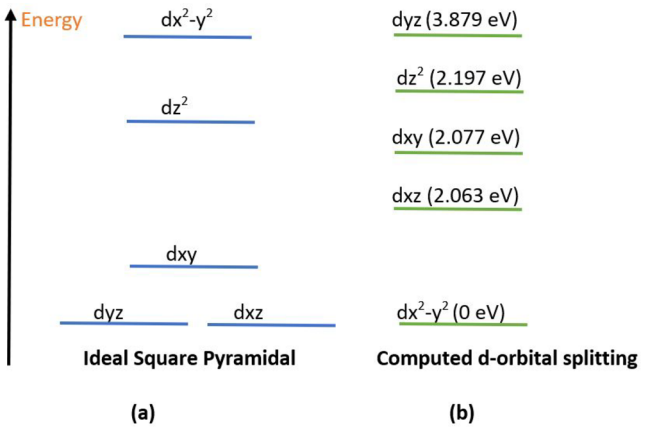

Figure 2. Energy level splitting of (a) an ideal square pyramidal structure and (b) the vanadium(IV) center. Energy level splittings were calculated with the AILFT module in the ground-state wave function.

From the CAS-SCF block, the coefficient of contribution for multiple configurations can be exactly noted down. The root 0 (ground state) wave function is made up of

$$|\Psi_{gs}\rangle = \sqrt{0.55}\,|\Phi_1\rangle + \sqrt{0.24}\,|\Phi_2\rangle + \sqrt{0.19}\,|\Phi_3\rangle + \sqrt{0.01}\,|\Phi_4\rangle + \sqrt{0.003}\,|\Phi_5\rangle$$

where every $|\phi_1\rangle$ is the representation of a different electronic configuration.

Supporting Information Table S9 contains the respective information on the electronic configurations of all electronic states. Further, the Racah parameter, *B*, comes out to be zero, essentially meaning there is no electron−electron repulsion. This is already evident from the fact that there is only one electron in the active space.

After the structural study and its effect on the energy levels of central metal, the better bonding nature in complex **1** was analyzed using NBO calculations (see Figure 3).[44] The V(IV)−O bond has an occupancy of 0.98, which is polarized toward the oxygen atom (75%) (see Table 2). Major participation of d-orbitals was observed for the vanadium(IV) atom, whereas the p-orbital contribution dominated in the oxygen atom. The negative value of the natural charge on oxygen suggests that the electron density flows from vanadium to the oxygen ligand. Molecular orbital analysis denotes the presence of an unpaired electron in the α-SOMO (d_{yz}) orbital. α-SOMO-1 and α-SOMO-2 represent the lone-pair orbitals on the respective oxygen atoms. α-SOMO-4 denotes the hydrogen bonding interaction between the hydrogen atom of the displaced water molecule and the oxygen atom (connected with the phosphorus atom). α-LUMO+2 and α-LUMO+3 indicate the presence of vacant d_{xy} orbitals on the neighboring V(V) metal atoms (see Figure 4).[45]

Table 2. NBO Results for $[H_6(V^{IV}O_2)(V^{V}_2O_5)_2R_2]^{4-}$[R= O_3P-C(O)(CH_2-2-C_5NH_4)-PO_3] (1) in the Doublet State[a]

complex	bond	ON	polarization and hybridization (%)		WBI	*q* on O
1	V−O	0.98	V: 25 s(4.4), p(15.5), d(80.1)	O: 75 s(5.4), p(94.6)	0.53	−0.445
	V−O	0.98	V: 25 s(12), p(8), d(80)	O: 75 s(16.3), p(83.7)		
	V−O	0.98	V: 25 s(4), p(15.4), d(80.6)	O: 75 s(4.7), p(95.3)		

[a]Calculated at the BP86/Def2TZVPP level of theory using water as the solvent medium. ON = occupation number. *q* = partial charge.

2.2. Magnetic Property Study. The static and dynamic magnetic properties of the complexes $(NH_4)_4[H_6(V^{IV}O_2)(V^{V}_2O_5)_2\{O_3P\text{-}C(O)(CH_2\text{-}2\text{-}C_5NH_4)\text{-}PO_3\}_2]\cdot 9H_2O$ (**1**) and $(NH_4)_4[H_6(V^{IV}O_2)(V^{V}_2O_5)_2\{O_3P\text{-}C(O)(CH_2\text{-}3\text{-}C_5NH_4)\text{-}PO_3\}_2]\cdot 8H_2O$ (**2**) were studied with a superconducting quantum interference device (SQUID) magnetometer. Since both complexes **1** and **2** are iso-structural, except for a slight change in the orientation of the ligand, and contain the same magnetically active V(IV) atom(s) with similar coordination environments, both complexes exhibit similar trends in their magnetization dynamics. Therefore, we discuss the magnetic properties of complex **1** here, and the magnetic properties of complex **2** are discussed in the Supporting Information.

The variable-temperature DC magnetic susceptibility measurements were performed with a polycrystalline sample of **1** under an applied DC field of 1000 Oe in the temperature range of 2−300 K (see Supporting Information Figure S3). The $\chi_M T$ value of 0.38 cm^3 K mol^{-1} obtained at 300 K is close to the theoretically calculated value of 0.35 cm^3 K mol^{-1} for a single isolated V^{IV} metal ($3d^1$, $S = 1/2$, $^2D_{3/2}$ and $g = 1.930$).[46] This almost equal value suggests the absence of spin−orbit coupling or any external interference. The expression used to calculate the $\chi_M T$ product theoretically is given in eq 1

$$\chi_M T = \frac{g^2}{8} S(S+1) \quad (1)$$

The $\chi_M T$ value under an applied field of 1000 Oe was also calculated to verify the experimentally observed susceptibility product values. At a temperature as low as 2 K, the $\chi_M T$ value was found to be 0.359 cm^3 K mol^{-1}, whereas at room

https://doi.org/10.1021/acs.cgd.2c00754
Cryst. Growth Des. 2022, 22, 5666−5679

temperature the value increased linearly to 0.373 cm^3 K mol^{-1} (see Supporting Information Figure S4). All three $\chi_M T$ values at 300 K are compared in Table 3.

Table 3. $\chi_M T$ values at 300 K for $[H_6(V^{IV}O_2)(V^{V}{}_2O_5)_2\{O_3P\text{-}C(O)(CH_2\text{-}2\text{-}C_5NH_4)\text{-}PO_3\}_2]^{4-}$ (1)

	method		
parameter	theoretically expected	experimentally observed	computationally calculated
$\chi_M T$ (cm^3 K mol^{-1})	0.35	0.38	0.373

These values match the $\chi_M T$ values of $S = 1/2$ systems reported in the literature.[47] Upon cooling, the experimental $\chi_M T$ value slowly decreases to become 0.34 cm^3 K mol^{-1} at 240 K. The $\chi_M T$ value remains almost same upon further cooling and becomes 0.32 cm^3 K mol^{-1} at 2 K. There are no other paramagnetic metal centers around the V(IV) atom in the polyanionic complex **1**; hence, no exchange interactions were observed within the system. The correlation between the experimental and computational field dependence of molar magnetization at different temperatures (see Supporting Information Figures S5 and S6) is obviously not exact, however the values are definitely in very close proximity (see Supporting Information Table S12). The magnetization in the low field limit shows linear behavior, but after a certain threshold of applied field the path becomes nonlinear. This threshold field is different for different temperature data sets. As long as the magnetization changes with the variation in the field, the magnetic moments are still in a state of flux such that they still align themselves with respect to the field. At an applied field of 7 T and a temperature of 2 K, the saturation point was almost reached for the experimental and computational data sets, with values of 0.88 and 0.96 μ_B, respectively. This saturation point is known as the ceiling of magnetization for complex **1** for that particular temperature.

As mentioned earlier, since the mixed-valent structure of complex **1** contains four diamagnetic vanadium(V) atoms and a solitary paramagnetic vanadium(IV) atom, the unpaired electron on the central vanadium(IV) ($S = 1/2$) atom gives the molecule its magnetic moment, which is responsible for reversal of its magnetization or spin at low temperatures. This unique mixed-valent assembly is stabilized by the organic diphosphonate ligand, with the vanadium(IV) atom having a six-coordinate distorted octahedral environment while the

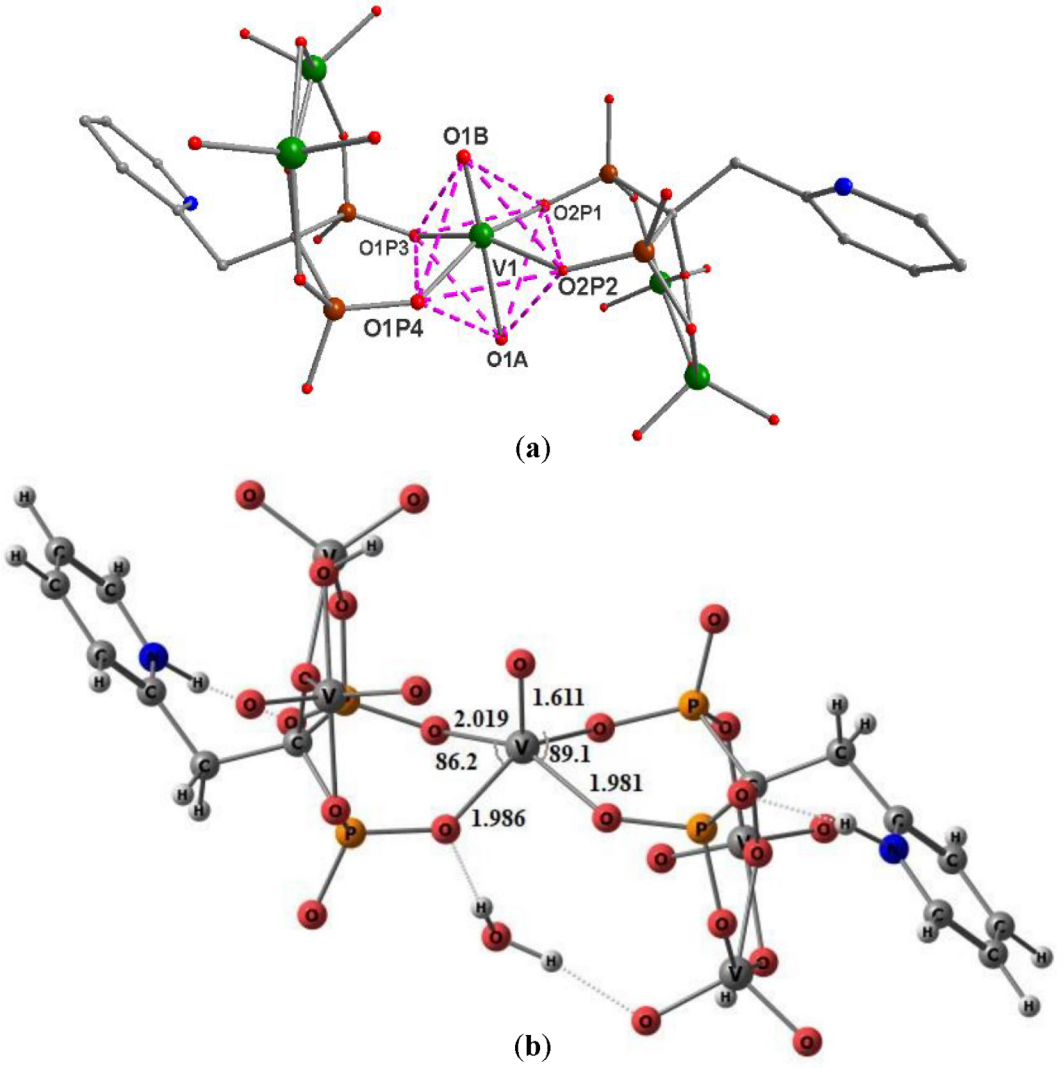

Figure 3. (a) Molecular and (b) NBO-optimized structures of $[(V^{IV}O_2)(V^{V}{}_2O_5)_2\{O_3P\text{-}C(O)(CH_2\text{-}2\text{-}C_5NH_4)\text{-}PO_3\}_2]^{4-}$ (**1**).

https://doi.org/10.1021/acs.cgd.2c00754
Cryst. Growth Des. 2022, 22, 5666−5679

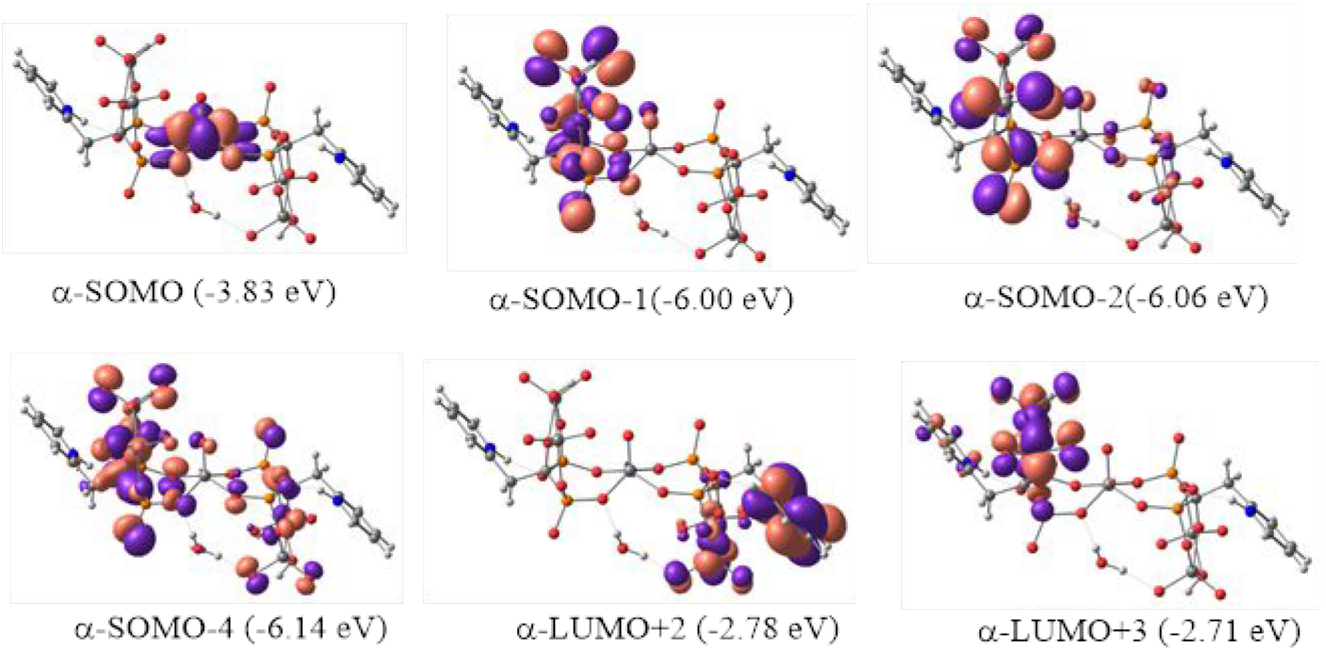

Figure 4. SOMO LUMO pictures obtained from NBO calculations of $[(V^{IV}O_2)(V^{V}{}_2O_5)_2\{O_3P\text{-}C(O)(CH_2\text{-}2\text{-}C_5NH_4)\text{-}PO_3\}_2]^{4-}$ (**1**).

vanadium(V) atoms have a five-coordinate distorted square pyramidal environment, essentially leading to the formation of the ($V^{V}{}_2O_5$) dimeric unit(s) within the structure (vide supra). The entire magnetic property of polyanion complex **1** thus stems from the solitary vanadium(IV) atom present. Therefore, to understand the magnetization dynamics of **1**, AC susceptibility measurements were performed. Under zero DC field, no imaginary component (χ'') of the magnetic susceptibility was observed up to the lowest investigated temperature of 2 K (see Supporting Information Figure S7). Being a Kramers ion with $S = 1/2$, V^{IV} produces one Kramer doublet, which essentially means that the system has at least two degenerate-energy eigen states. The advantage of having a Kramers system over non-Kramers system is that a half-integer spin state should be able to minimize the quantum tunneling effect,[48] which goes on to help improve the SIM properties. In the absence of higher Kramers doublets, i.e., integer half-spin molecules with $S > 1/2$ or a spin multiplicity >3 in the ground state, the Orbach process-assisted slow relaxation of spin states is prohibited at zero DC field,[29] due to the absence of an effective energy barrier against the spin reversal. Hence, the molecule shows fast relaxation of magnetization at zero field, which is made possible with the help of direct and quantum tunnelling relaxation effects. This can be effectively proven with the computationally obtained energy of spin eigen states by calculating the energy barrier (see Supporting Information Figure S20). Usually, the computing energy barrier of states directly gives us an idea of ZFS parameters D and E, i.e., axial and orthorhombic parameters, respectively. They enter the spin Hamiltonian formalism and define the spin−spin interaction under zero-field when $S > 1/2$. The spin Hamiltonian can be expressed by eq 2.

$$\hat{H}_{1/2} = D\left(\hat{S}_Z^2 - \frac{1}{3}\hat{S}^2\right) + E(\hat{S}_X^2 - \hat{S}_Y^2) \tag{2}$$

The ab initio energy barrier graph computed at zero field (see Supporting Information Figure S20) verifies that the spin eigen states are present at 0 cm^{-1} energy, which implies that this spin system has no energy barrier; hence, very fast relaxation between opposite spin magnetic moments is observed. This also means that the D and E parameters are nonexistent and therefore cannot be computed.

However, upon the application of a static magnetic field, the degenerate energy levels are split up and relaxation mechanisms such as direct, thermal, and Raman relaxation processes could occur.[49] Therefore, slow relaxation of magnetization is induced upon the application of a static field, which manifest in the form of an increase in the peak in the imaginary component (χ'') of the susceptibility and a concomitant decrease of the real component of the susceptibility (χ') (see Figure 5a and 5b). The optimal external field was found to be 3400 Oe (see Supporting Information Figure S8); therefore, AC susceptibility measurements were performed at H_{DC} = 3400 Oe in the temperature range of 2−10 K. The thermal dependence of the AC susceptibility was also judged based on the shift of the maximum of the imaginary AC susceptibility component with the change in temperature. The discussed α-parameters and relaxation times were obtained by simultaneously fitting χ' and χ'' to a generalized Debye model.

The Cole−Cole plots (χ'' vs χ') obtained within the temperature range of 2−10 K possess an asymmetric semicircular shape with low α values in the range of 0.06−0.23, implying a narrow distribution of relaxation times and suggesting presence of wider relaxation regimes in the system (see Figure 6). Generally, for a slow relaxation phase, the α values (>0) are higher and are distributed in a wider range.[50] As previously pointed out, for a system with one Kramers pair spin state, the energy barrier is bound to be negligible. To verify this point for certainty with experimental data set, the energy barrier against the spin reversal of magnetization was estimated by fitting the relaxation time variation with temperature (see Figure 7a) using the Orbach relaxation shown in eq 3.

https://doi.org/10.1021/acs.cgd.2c00754
Cryst. Growth Des. 2022, 22, 5666−5679

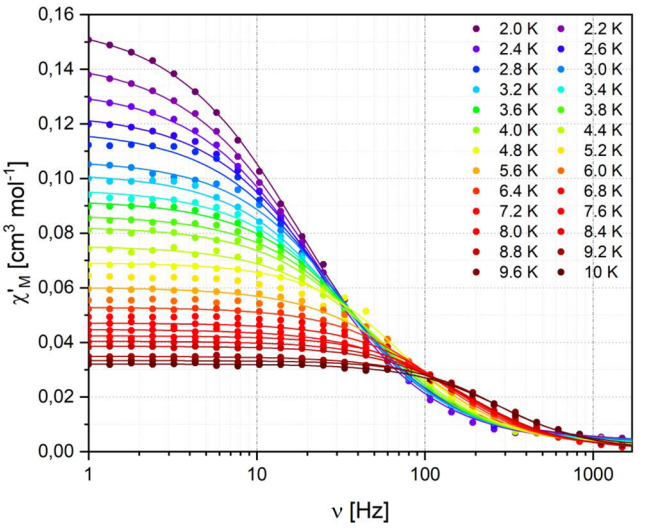

(a)

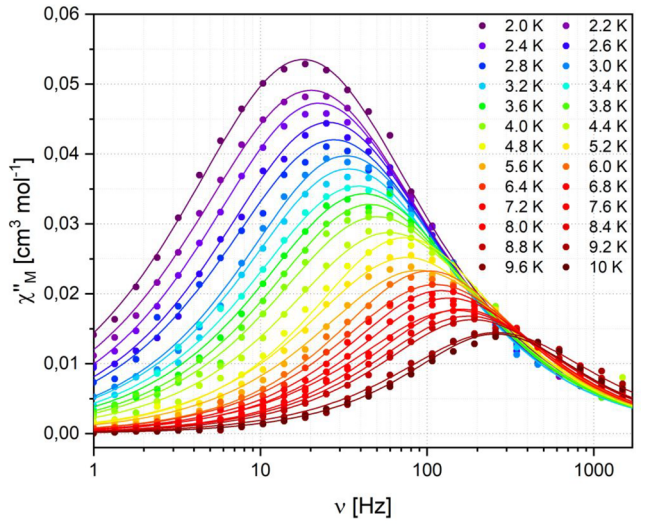

(b)

Figure 5. (a) In-phase, and (b) out-of-phase AC susceptibility parameters obtained for $(NH_4)_4[H_6(V^{IV}O_2)(V^{V}{}_2O_5)_2\{O_3P\text{-}C(O)(CH_2\text{-}2\text{-}C_5NH_4)\text{-}PO_3\}_2]\cdot 9H_2O$ (**1**) plotted against the frequency (Hz) at various temperatures under applied H_{DC} = 3400 Oe. Solid lines represent the best fit determined using a Debye model.

$$\ln(\tau) = \ln(\tau_O) + \frac{\Delta E}{k_B T} \tag{3}$$

Here ΔE and τ_o are the parameters entering in the equation as the energy barrier and the relaxation time at 0 K, respectively.

For complex **1**, the values of the parameters extracted after fitting, estimates the energy barrier and τ_o at 4.71 cm^{-1} and 0.45 ms, respectively. The energy barrier is almost negligible and therefore the reversal of the spin will not depend on the Orbach-directed path for the dominant relaxation process. Thereafter, with a more considerate look at the nature of the relaxation time (τ) versus temperature plot, the curve was fitted with the equations of direct and raman relaxation processes using eq 4.

$$\tau^{-1} = aT + bT^n \tag{4}$$

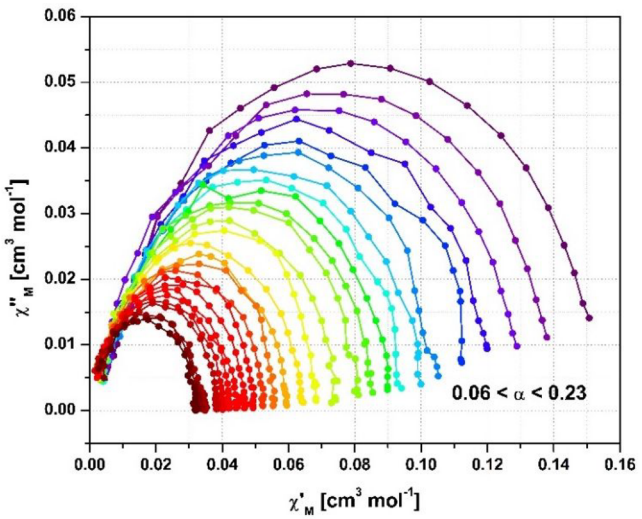

Figure 6. Cole−Cole plot for $(NH_4)_4[H_6(V^{IV}O_2)(V^{V}{}_2O_5)_2\{O_3P\text{-}C(O)(CH_2\text{-}2\text{-}C_5NH_4)\text{-}PO_3\}_2]\cdot 9H_2O$ (**1**) (H_{DC} = 3400 Oe). Solid lines are a guides for the eye.

The graph of τ^{-1} (s^{-1}) versus T (K) gave the parameters a, b, and n, where the a (64.82 s^{-1} K^{-1}) parameter estimates the direct process contribution and the b (= 0.58 s^{-1} K^{-n}) and n (= 3.27) parameters estimate the contribution of the Raman process in the overall field-induced slow relaxation of magnetization (see Figure 7b).

In the graph, the almost linearity of the plot verifies the dominance of the direct process, although at temperature above 6 K the plot behavior changes to an exponential curvature, which essentially indicates the dominance of the Raman process beyond this temperature. Since the behavior of the plot never shows temperature independence in the whole thermal range, the possibility of quantum tunneling of magnetization between the $\pm M_s$ spin states is completely ruled out.

Another way to explain the slow relaxation time of magnetization, qualitatively, is to quantify the g-tensor components of the SIM,[51] which aid the anisotropic understanding of a magnet. From previous studies, it has been established that the spin of the system alone is not able to justify and predict the magnetic behavior of the SIM. Therefore, we have come to the view that maximum anisotropy is a good parameter with which to judge the SIM behavior.[51] The components of the g-tensor can be computationally extracted by calculating the Zeeman interaction (interaction of the electronic magnetic moment with the magnetic field) entering the effective Spin Hamiltonian formalism, which is given by eq 5.

$$\hat{H}_{1/2} = \mu_B B_O g_{iso} \hat{S} \tag{5}$$

The two components of $g_\perp$ (g_{xx} and g_{yy}) and $g_\parallel$ (g_{zz}) represent the g-tensors of the molecule perpendicular to and along the applied magnetic field, respectively. The derived g_{xx} = 1.982802, g_{yy} = 1.981447, g_{zz} = 1.9199, and g_{iso} = 1.961401 values, with the largest g-shift in g_{zz} principle axis direction (see Supporting Information Table S11), reveal that the molecule does not contain a pure easy axis or exhibit easy plane anisotropic behavior.[51] Rather, there exists a rhombic distribution of the magnetic moment in the system.[52] For the pictorial vector representation of the g-tensor along its

https://doi.org/10.1021/acs.cgd.2c00754
Cryst. Growth Des. 2022, 22, 5666−5679

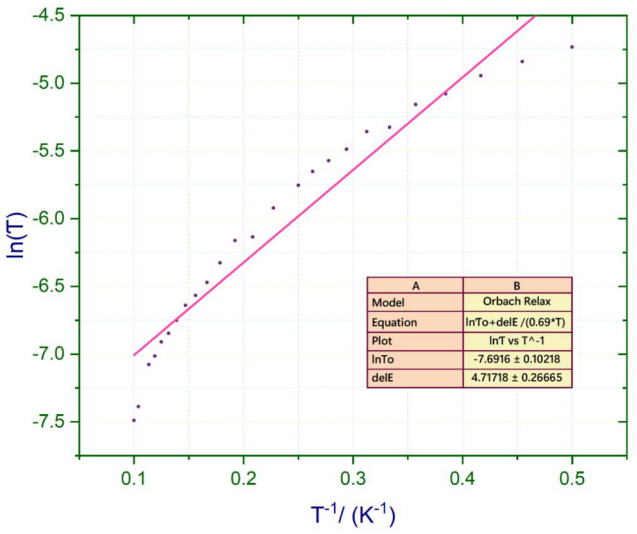

(a)

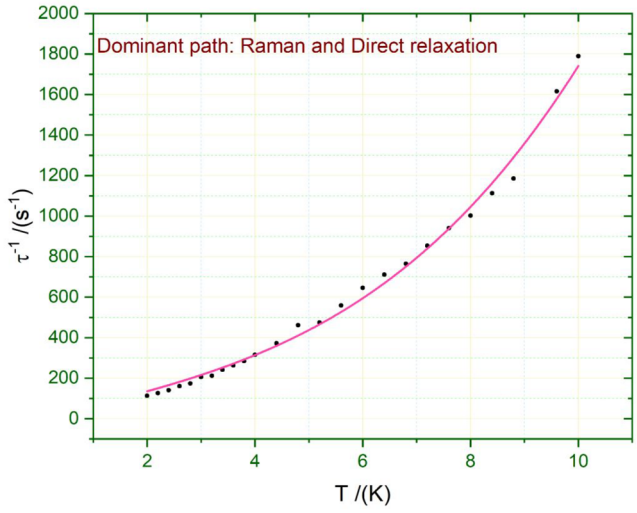

(b)

Figure 7. Temperature dependence of the magnetic relaxation time τ under H_{DC} = 3400 Oe for $[H_6(V^{IV}O_2)(V^{V}{}_2O_5)_2\{O_3P\text{-}C(O)(CH_2\text{-}2\text{-}C_5NH_4)\text{-}PO_3\}_2]^{4-}$ (**1**). Temperature dependence is shown as (a) $\ln(\tau)$ vs T^{-1} (K^{-1}), and (b) τ^{-1} (s^{-1}) vs T (K).

principle axes, we used computationally obtained eigen vectors (see Figure 8). The molecules that possess an easy-axis anisotropy exhibit better SIM properties in comparison to those with easy-plane anisotropy.[51,53] The value of the *g*-tensor computed for the optimized geometry of complex **1** is consistent with previously reported V(IV) single-ion magnets, such as the range of the previously reported five coordinated vanadium complex $VO(dpm)_2$.[22,54]

To further characterize the magnetic property of the complex with respect to temperature, the magnetic ordering in the complex was investigated with the help of χ_m data obtained both instrumentally and computationally. The Curie−Weiss expression is one of the most useful tools for quantifying the critical temperature or the Neel temperature of ferromagnetic or antiferromagnetic ordering, respectively.

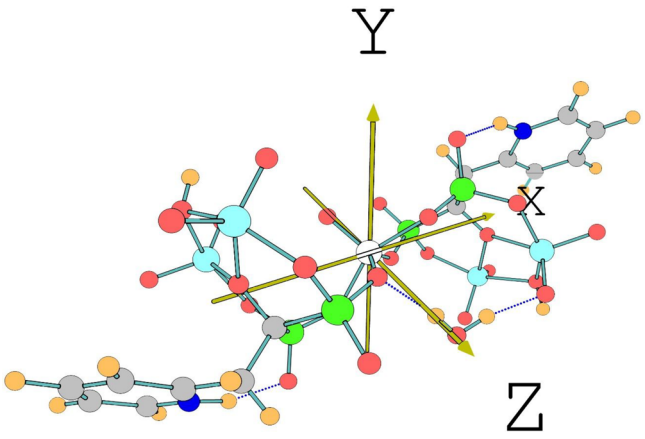

Figure 8. Orientation of the g-tensor components in the ground Kramer state for $[H_6(V^{IV}O_2)(V^{V}{}_2O_5)_2\{O_3P\text{-}C(O)(CH_2\text{-}2\text{-}C_5NH_4)\text{-}PO_3\}_2]^{4-}$ (**1**).

Hence, it is being used here to explain the anomalous magnetic behavior at low temperatures.

$$\chi_m^{-1} = \frac{T - \theta}{C} \tag{6}$$

Here C is the Curie constant and θ is the Weiss constant.

The graph of χ_m^{-1} versus T was plotted and fitted using eq 6 (see Figure 9a and b for instrumental and computational data, respectively). θ was found to be negative in both analytical methods (see Table 4), indicating the presence of antiferromagnetic ordering at low temperatures. Additionally, the Neel temperature (T_N) of the antiferromagnetic ordering is given as negative of θ. This could be due to the single-ion anisotropy of the V(IV) ion along with the weak intermolecular dipolar interactions.

2.3. Electron Paramagnetic Resonance Studies.

Electron paramagnetic resonance (EPR) spectra were recorded to understand the spin behavior of the metal atoms in complexes **1** and **2**. The $3d^1$ configuration of the central V(IV) atom creates a $S = 1/2$ system for both the complexes, where the spin density is dominantly localized on the vanadium(IV) atom (see Supporting Information Figure S9). The interaction between a magnetic field and the molecule is described by a simple spin Hamiltonian that includes only the Zeeman and hyperfine terms originating from the $I = 7/2$ nuclear spin of ^{51}V.[55] The hyperfine coupling visible in the spectrum is a consequence of the interaction between the electronic magnetic moment and the nuclear magnetic moment, which are given by the electronic and nuclear spin components eqs 7 and 8, respectively, as follows:

$$\mu_S = -g\mu_B\hat{S} \tag{7}$$

$$\mu_I = g_N\mu_N\hat{I} \tag{8}$$

where, μ_B is the Bohr magneton, μ_N is the nuclear magneton, $\hat{I}$ is the nuclear spin operator, $\hat{S}$ is the electronic spin operator, and g is the *g*-tensor,

Similarly, the Spin Hamiltonian for $S = 1/2$ systems is shown by eq 9.[56]

$$\hat{H}_{1/2} = g\mu_B\hat{S}\cdot B_O + \sum_j \hat{I}_j\bar{\bar{A}}\hat{S} \tag{9}$$

https://doi.org/10.1021/acs.cgd.2c00754
Cryst. Growth Des. 2022, 22, 5666−5679

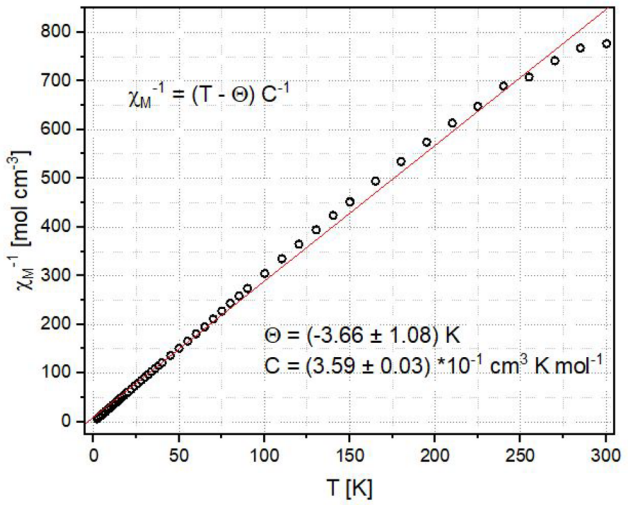

(a)

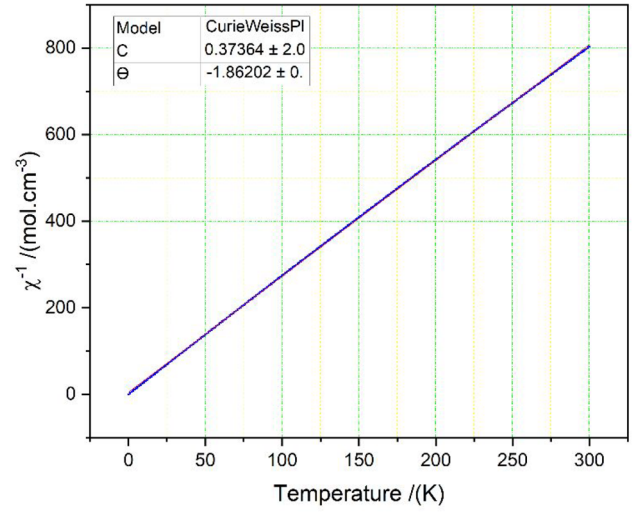

(b)

Figure 9. Curie–Weiss graph plotted with χ_m values obtained (a) instrumentally, and (b) computationally for $[H_6(V^{IV}O_2)(V^{V}_2O_5)_2\{O_3P\text{-}C(O)(CH_2\text{-}2\text{-}C_5NH_4)\text{-}PO_3\}_2]^{4-}$ (**1**).

Table 4. Comparison of Constants Derived from the Curie–Weiss Plots with the χm Value Obtained for $[H_6(V^{IV}O_2)(V^{V}_2O_5)_2\{O_3P\text{-}C(O)(CH_2\text{-}2\text{-}C_5NH_4)\text{-}PO_3\}_2]^{4-}$ (1)

parameters	instrumentally obtained	computationally derived
C	0.373	0.359
θ	−1.86	−3.66
T_N	1.86	3.66

Here A is the hyperfine tensor and B_O is the strength of the external magnetic field.

Since there is no electron–electron interaction present in the V^{IV} centers of polyanionic complexes **1** and **2**, electronic spin–spin interaction terms are not included in eq 9.

The room-temperature EPR spectrum of **2** in H_2O exhibit eight hyperfine lines (see Figure 10) as expected. Every line of the pattern consists of two peaks; hence, there is a total of 16 peaks. Every peak is an indication of a different energy level, which is obtained as a consequence of coupling between the

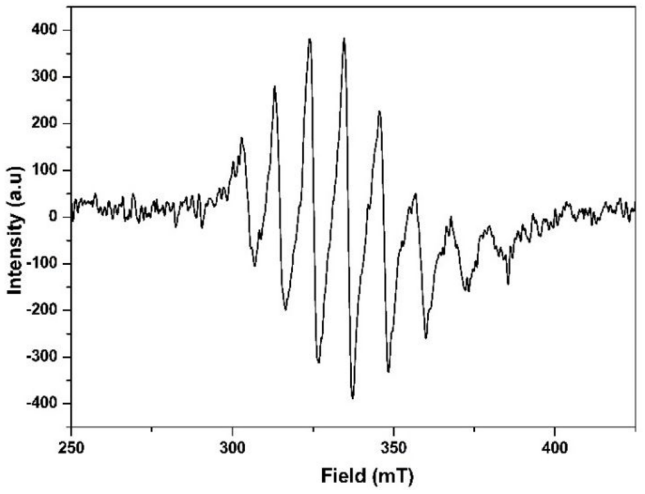

Figure 10. EPR spectrum of $[(V^{IV}O_2)(V^{V}_2O_5)_2\{O_3P\text{-}C(O)(CH_2\text{-}3\text{-}C_5NH_4)\text{-}PO_3\}_2]^{4-}$ (**2**) in aqueous solution.

$3d^1$ electron spin, S = 1/2 and the vanadium atom having spin active ^{51}V-nuclei with I = 7/2. Under the electromagnetic radiation impact, there would be transitions between energy states following the selection rule of $M_s = \pm 1$ and $M_I = 0$, which will give the expected eight lines observed in the spectrum. Therefore, the expression $(2S + 1)\cdot(2n_N I + 1)$ gives the total number of energy levels as 16, justifying the 8 line pattern obtained (see Figure 10).[57,58] To determine the g- and A-tensor values, the experimentally obtained EPR spectrum was simulated using "Easy Spin" (see Figure 11).

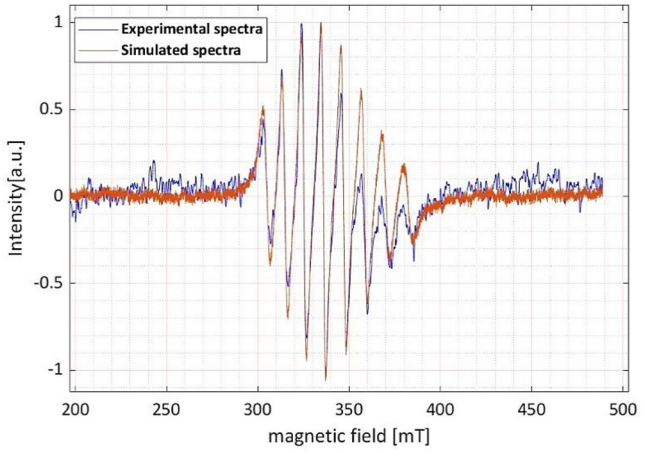

Figure 11. Computationally simulated solution-phase EPR spectrum of $[(V^{IV}O_2)(V^{V}_2O_5)_2\{O_3P\text{-}C(O)(CH_2\text{-}2\text{-}C_5NH_4)\text{-}PO_3\}_2]^{4-}$ (**2**).

The simulated spectrum takes the corresponding values: $g_{xx} = g_{yy} = 1.98$, $g_{zz} = 1.95$, $g_{iso} = 1.97$, $A_{XX} = 175$ MHz, $A_{YY} = A_{ZZ} = 370$ MHz, and $A_{ISO} = 305$ MHz, where the isotropic values are given by eqs 10 and 11. The reported g-values are consistent with the already studied V^{IV} system.[29]

$$g_{iso} = \frac{1}{3}(g_{XX} + g_{YY} + g_{ZZ}) \quad (10)$$

$$A_{ISO} = \frac{1}{3}(A_{XX} + A_{YY} + A_{ZZ}) \quad (11)$$

https://doi.org/10.1021/acs.cgd.2c00754
Cryst. Growth Des. 2022, 22, 5666−5679

In the solid-state EPR spectrum, two sets of eight lines are visible. However, the spectrum is distorted; therefore, the electron must be interacting with two different active nuclei to give two separate hyperfine constant values. The second interaction (other than the central vanadium atom nucleus) must be very weakly coupled, because the widths of the additional lines are not properly resolved. We have three possible nuclei to consider: ^{31}P and ^{1}H with $I = 1/2$, and ^{51}V with $I = 7/2$. Since there are four equivalent nuclei of ^{31}P and ^{51}V present in the system, the solid-state EPR spectrum is expected to show 40 and 224 lines as the consequence of transition between 80 and 448 Zeeman states, respectively, following the expression $(2S + 1)\cdot(2n_1I_1 + 1)\cdot(2n_2I_2 + 1)$. The recorded spectra for complexes **1** and **2** (see Supporting Information Figure S10 and Figure 12 for solid-state EPR spectra of complexes **1** and **2**, respectively) do not show this behavior, leaving coupling with the nearest proton to be the only plausible explanation. The hyperfine coupling with the nearest proton is bound to be weak given the fact that the central vanadium atom is four bonds away.[59]

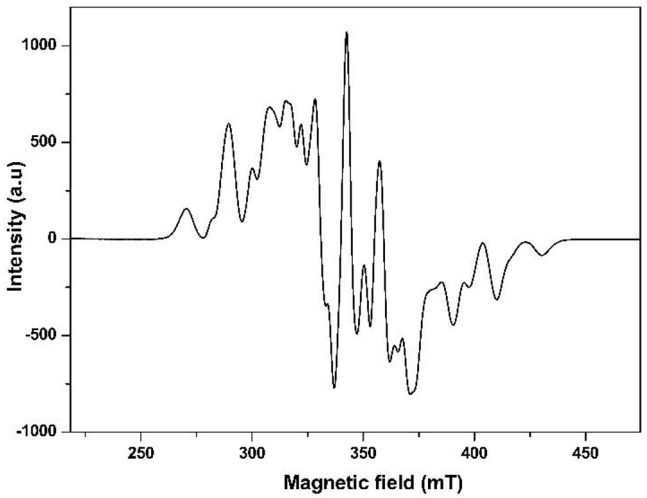

Figure 12. EPR spectrum of $[(V^{IV}O_2)(V^{V}{}_2O_5)_2\{O_3P\text{-}C(O)(CH_2\text{-}3\text{-}C_5NH_4)\text{-}PO_3\}_2]^{4-}$ (**2**) in the solid state.

3. MATERIALS AND METHODS

Synthesis of $(NH_4)_4[H_6(V^{IV}O_2)(V^{V}{}_2O_5)_2\{O_3P\text{-}C(O)(CH_2\text{-}2\text{-}C_5NH_4)\text{-}PO_3\}_2]\cdot 9H_2O$ (1). The complex was synthesized using a previously reported procedure.[27] In brief, to 0.1003 g of $V_2O_5\cdot xH_2O$ (0.5 mmol) taken in 10 mL of 2 M ammonium acetate buffer (pH 4.7), was added 0.1390 g of 1-hydroxy-2-(2-pyridyl) ethylidene-1,1-bisphosphonic acid (0.5 mmol). The solution was stirred at 80 °C for 30 min. Green crystals were collected after 20 days. Yield: 0.1021 g (20% based on V). Elemental analysis (%) Calcd for **1**: V, 20.49; P, 9.97; C, 13.53; H, 4.22; N, 6.76; O, 45.04. Found: V, 20.27; P, 9.85; C, 13.83; H, 3.72; N, 6.65; O, 45.56.

Synthesis of $(NH_4)_4[H_6(V^{IV}O_2)(V^{V}{}_2O_5)_2\{O_3P\text{-}C(O)(CH_2\text{-}3\text{-}C_5NH_4)\text{-}PO_3\}_2]\cdot 8H_2O$ (2). This complex was also synthesized using a previously reported procedure,[27] analogous with respect to that used for **1**, except 1-hydroxy-2-(2-pyridyl) ethylidene-1,1-bisphosphonic acid was subsituted with 1-hydroxy-2-(3-pyridyl) ethylidene-1,1-bisphosphonic acid. Yield: 0.1526 g (50% based on V). Elemental analysis (%) Calcd for **2**: V, 20.79; P, 10.11; C, 13.72; H, 4.11; N, 6.86; O, 44.40. Found: V, 20.61; P, 9.90; C, 13.66; H, 3.48; N, 6.34; O, 44.50.

Single-Crystal X-ray Diffraction Analysis. Single crystals of **1** and **2** were mounted on a Bruker AXS (D8 Quest System) X-ray diffractometer equipped with a PHOTON 100 CMOS detector using Mo Kα radiation (λ = 0.71073 Å) at 293(2) K. Direct methods were used to solve the structures and locate the heavy atoms (SHELXS97), and the remaining atoms were found from successive difference maps (SHELXL97).[60] Routine Lorentz and polarization corrections were applied, and an absorption correction was performed using the SADABS program.[61] The hydrogens of all the C and O atoms were added in calculated positions and refined using a riding model. Crystallographic data are summarized in Supporting Information Table S1. CCDC 2018570 and 2018571 contain the supplementary crystallographic data for complexes **1** and **2**. These data can be obtained free of charge via www.ccdc.cam.ac.uk/data_request/cif, or by emailing data_request@ccdc.cam.ac.uk, or by contacting The Cambridge Crystallographic Data Centre, 12 Union Road, Cambridge CB2 1EZ, UK; fax: + 44 1223 336033.

Powder X-ray Diffraction Analysis. Powder X-ray diffraction (PXRD) studies were performed to determine the phase purity of the complexes [see Figures S1 and S2 in Supporting Information for **1** and **2**, respectively]. PXRD data was collected on Bruker D8ECO with Cu Kα source radiation (λ = 1.54056 Å) from angular range 5−50° at 298 K.

Elemental Analysis Studies. Elemental analysis data were used to determine accurate formulas for the complexes. Elemental analysis for C, H, N, and O was performed on a Thermo Scientific Flash 2000 Organic Elemental Analyzer (CHNS/O Mode). Elemental analysis for V and P was performed using a quadrupole inductively coupled plasma-mass spectrometer (ICP-MS, Thermo X Series II).

Magnetism Studies. Temperature-dependent susceptibility and AC susceptibility measurements were carried out on a Quantum Design MPMS-XL 3 SQUID magnetometer. M_H data were collected on a Quantum Design MPMS3 VSM magnetometer. The polycrystalline samples were ground to a powder and fixed in a gelatin capsule. All data were corrected for diamagnetic contributions of the sample holder and the sample itself using Pascal's constants.

Electron Paramagnetic Resonance Studies. The X-band EPR spectra were recorded with JEOL JES-FA series at 9.45 GHZ, and both complexes **1**−**2** were measured in solid and solution phase. Solution-phase EPR spectra data for **1** were not recorded, ostensibly due to poor solubility.

Computational Studies. Complexes $(NH_4)_4[H_6(V^{IV}O_2)(V^{V}{}_2O_5)_2\{O_3P\text{-}C(O)(CH_2\text{-}2\text{-}C_5NH_4)\text{-}PO_3\}_2]\cdot 9H_2O$ (**1**), and $(NH_4)_4[H_6(V^{IV}O_2)(V^{V}{}_2O_5)_2\{O_3P\text{-}C(O)(CH_2\text{-}3\text{-}C_5NH_4)\text{-}PO_3\}_2]\cdot 8H_2O$ (**2**) are structurally similar. It is hard to locate the positions of the protons to charge balance such materials. However, the central V(IV) center is $S = 1/2$ with a double-bonded O atom ($O{=}V^{IV}$, 1.582 Å) and a weakly bonded H_2O molecule ($V^{IV}{-}OH_2$, 2.363 Å in the solid state) on the opposite site. We optimized the experimentally characterized vanadium complex $[H_6(V^{IV}O_2)(V^{V}{}_2O_5)_2R_2]^{4-}$ [R = $\text{-}O_3P\text{-}C(O)(CH_2\text{-}2\text{-}C_5NH_4)\text{-}PO_3$] (**1**) in the doublet state at the BP86/Def2-TZVPP level of theory using water as the solvent medium [Figure 1].[62−67] The optimized geometry has a five-coordinate paramagnetic vanadium(IV) center, and a six-coordinate H_2O ligand dissociates away from central metal and subsequently bonds within the complex sphere by hydrogen bonding. To optimize the geometry of complex **1** at the BP86 level, the state-averaged CASSCF with the Ahlrichs polarized basis set def2-tzvpp[63,64] was used with the ORCA 5.0.0. package.[68] The auxiliary basis set def2-tzvpp/c was used in conjunction with the RI approximation. Since we are using a wave function-based theory and dealing with the movement of large set of electrons, it is necessary to consider relativistic corrections in the computation of the molecule to improve the accuracy and reliability of the data. To recover the majority of the dynamic correlation, we use a substantially constricted version of *N*-electron valence perturbation theory to second-order (NEVPT2-SC).[68] The Douglas−Kroll−Hess procedure was used to account for scalar relativistic effects. The active space chosen for the CASSCF calculation was CAS (1,5), i.e., one electron in five 3d orbitals of the central vanadium(IV) metal. All five roots arising from ^{2}D ground state term of vanadium(IV) were considered. Dynamic correlation was included through NEVPT2 approximations; only the perturbed energies were

https://doi.org/10.1021/acs.cgd.2c00754
Cryst. Growth Des. 2022, 22, 5666−5679

entered in the calculations while the wave functions remained at the CASSCF level. The EPR parameters of the considered complexes were also calculated using the same methods with an effective spin Hamiltonian and a quasi-degenerate perturbation theory (QDPT) approach. Using the SINGLE_ANISO module, the DC magnetic susceptibility was computed at an applied field of 0.1 T. For the EPR simulation, Easy Spin software was used.[69]

4. CONCLUSION

We have investigated the electronic, magnetic, and EPR spectroscopic properties of two organo-polyoxovanadate complexes, $(NH_4)_4[H_6(V^{IV}O_2)(V^{V}_2O_5)_2\{O_3P\text{-}C(O)(CH_2\text{-}2\text{-}C_5NH_4)\text{-}PO_3\}_2]\cdot 9H_2O$ (**1**) and $(NH_4)_4[H_6(V^{IV}O_2)\text{-}(V^{V}_2O_5)_2\{O_3P\text{-}C(O)(CH_2\text{-}3\text{-}C_5NH_4)\text{-}PO_3\}_2]\cdot 8H_2O$ (**2**). Each of the complexes consists of two types of vanadium-oxo fragments, namely, one $\{V^{IV}O_6\}$ fragment and two $\{V_2{}^{V}O_5\}$ fragments. The central vanadium(IV) atom was observed to be hexa-coordinated in the crystal structure, with significant axial distortion. However, upon optimization to find the equilibrium geometry, taking water as the solvent medium at the BP86/Def2TZVPP level of theory, the vanadium(IV) atom was left as a penta-coordinate center. DC and AC magnetic susceptibility measurements in the solid-state in the temperature range of 2−300 K were performed to shed light on the dynamic magnetic properties of both the complexes. The maxima in the "out-of-phase" magnetic susceptibility plotted against frequency (χ'' vs ν), obtained at an applied static field of 3400 Oe, suggest the presence of slow relaxation of spin. Owing to the single electron and one Kramers doublet system, such a complex effectively does not have any energy barrier and consequently will not have any zero-field splitting contribution to the anisotropy. Hence, to justify the anisotropy and SIM behavior, we depended on the *g*-tensor quantification and visualization, which revealed the system to be neither easy axis nor easy plane but instead somewhere in between.[17,18] The fitting of τ^{-1} versus T suggests that the low-temperature (2−6 K) and high-temperature (6−10 K) domains of relaxations are dominated by direct and multiphonon Raman processes, respectively. The EPR spectrum in solution-phase at room temperature of the polyanionic complex **2** has eight hyperfine lines, which is in perfect agreement with a $S = 1/2$ system involved in a hyperfine interaction with a $I = 7/2$ vanadium nucleus. Meanwhile, the solid-state EPR spectrum shows two sets of eight hyperfine lines, suggesting that the system potentially also interacts with a neighboring proton/phosphorous nucleus, which is four bonds away from the central vanadium. The EPR spectra were simulated to get an idea of the values of the *g* and *A*-tensors. The simulated *g*-tensor values were found to be in accordance with previously reported studies; however, the *A* tensor values deviated a bit, perhaps due to unusual anisotropy in the systems under investigation. The slow relaxation of magnetizations of complexes **1** and **2** are comparable to those of pentacoordinate V^{IV} complexes recently reported for their unusually slow relaxation time.[17,18]

■ ASSOCIATED CONTENT

Supporting Information

The Supporting Information is available free of charge at https://pubs.acs.org/doi/10.1021/acs.cgd.2c00754.

Crystal data and structure refinement parameters, bond-valence sum calculations, relevant bond distances, relevant bond angles, comparative powder XRD patterns, temperature dependence plots, field-dependent magnetization, out-of-phase vs frequency plots, optimization of the external field, spin density and EPR spectrum of **1**, magnetic properties of **2**, Cole−Cole plot of **2**, computed ligand field eigenfunction table, d^1 configurations of slater determinants in the ground state, matrix elements, comparison of computation and experimental molar magnetization data, and computed parameters (PDF)

Accession Codes

CCDC 2018570−2018571 contain the supplementary crystallographic data for this paper. These data can be obtained free of charge via www.ccdc.cam.ac.uk/data_request/cif, or by emailing data_request@ccdc.cam.ac.uk, or by contacting The Cambridge Crystallographic Data Centre, 12 Union Road, Cambridge CB2 1EZ, UK; fax: +44 1223 336033.

■ AUTHOR INFORMATION

Corresponding Authors

Kartik Chandra Mondal − *Department of Chemistry, Indian Institute of Technology Madras, Chennai, Tamil Nadu 600036, India;* orcid.org/0000-0002-5830-3608; Email: csdkartik@iitm.ac.in

Abhishek Banerjee − *Department of Chemistry, Visvesvaraya National Institute of Technology, Nagpur, Maharashtra 440010, India;* orcid.org/0000-0003-4552-4820; Email: abhishekbanerjee@chm.vnit.ac.in

Authors

Pragyansh Singh − *Department of Chemistry, Indian Institute of Technology Madras, Chennai, Tamil Nadu 600036, India*

Sören Schlittenhardt − *Institute of Nanotechnology (INT), Karlsruhe Institute of Technology, Eggenstein-Leopoldshafen, Baden-Württemberg 76344, Germany*

Dewendra Thakre − *Department of Chemistry, Visvesvaraya National Institute of Technology, Nagpur, Maharashtra 440010, India*

Saroj Kumar Kushvaha − *Department of Chemistry, Indian Institute of Technology Madras, Chennai, Tamil Nadu 600036, India*

Sunil Kumar − *Department of Chemistry, Indian Institute of Technology Madras, Chennai, Tamil Nadu 600036, India*

Harsha S. Karnamkkott − *Department of Chemistry, Indian Institute of Technology Madras, Chennai, Tamil Nadu 600036, India*

Mario Ruben − *Institute of Nanotechnology (INT), Karlsruhe Institute of Technology, Eggenstein-Leopoldshafen, Baden-Württemberg 76344, Germany; Institute of Quantum Materials and Technologies (IQMT), Karlsruhe Institute of Technology, Eggenstein-Leopoldshafen, Baden-Württemberg 76344, Germany; Centre Européen de Science Quantique (CESQ), Institut de Science et d'Ingénierie Supramoléculaires (ISIS, UMR 7006), CNRS-Université de Strasbourg, Strasbourg Cedex 67083, France*

Masooma Ibrahim − *Institute of Nanotechnology (INT), Karlsruhe Institute of Technology, Eggenstein-Leopoldshafen, Baden-Württemberg 76344, Germany;* orcid.org/0000-0002-8520-8585

Complete contact information is available at: https://pubs.acs.org/10.1021/acs.cgd.2c00754

https://doi.org/10.1021/acs.cgd.2c00754
Cryst. Growth Des. 2022, 22, 5666−5679

Author Contributions

P.S.: methodology, formal analysis, investigation, data curation, and writing (original draft). S.S.: methodology, formal analysis, investigation, data curation, and writing (review and editing). D.T.: methodology, formal analysis, investigation, data curation, and writing (review and editing). S.K.: methodology, formal analysis, investigation, data curation, and writing (original draft). S.K.: methodology, formal analysis, investigation, data curation, and writing (review and editing). H.S.K.: methodology, formal analysis, investigation, data curation, and writing (review and editing). M.R.: conceptualization, writing (review and editing), and supervision. M.I.: conceptualization, writing (review and editing), and supervision. A.B.: conceptualization, writing (review and editing), supervision, and funding acquisition. K.C.M.: conceptualization, writing (review and editing), supervision, and funding acquisition.

Notes

The authors declare no competing financial interest.

■ ACKNOWLEDGMENTS

A.B. thanks SERB (Grant ECR/2017/000932) and CSIR (Grant 01(3004)/19/EMR-II) for financial assistance. K.C.M. thanks SERB for the ECR Grant (ECR/2016/000890). The authors are grateful to DST-FIST (SR/FIST/CSI-279/2016(C)) for providing the characterization facility.

■ REFERENCES

(1) Lis, T. Preparation, structure, and magnetic properties of a dodecanuclear mixed-valence manganese carboxylate. *Acta Crystallogr.* **1980**, *B36* (9), 2042−2046.
(2) Soler, M.; Wernsdorfer, W.; Folting, K.; Pink, M.; Christou, G. Single-molecule magnets: a large Mn30 molecular nanomagnet exhibiting quantum tunneling of magnetization. *J. Am. Chem. Soc.* **2004**, *126* (7), 2156−2165.
(3) Bogani, L.; Wernsdorfer, W. Molecular spintronics using single-molecule magnets. *Nat. Mater.* **2008**, *7* (3), 179−186.
(4) Sessoli, R. Toward the Quantum Computer: Magnetic Molecules Back in the Race. *ACS Cent. Sci.* **2015**, *1* (9), 473−474.
(5) Gaita-Ariño, A.; Luis, F.; Hill, S.; Coronado, E. Molecular spins for quantum computation. *Nat. Chem.* **2019**, *11* (4), 301−309.
(6) Atzori, M.; Sessoli, R. The Second Quantum Revolution: Role and Challenges of Molecular Chemistry. *J. Am. Chem. Soc.* **2019**, *141* (29), 11339−11352.
(7) Moreno-Pineda, E.; Godfrin, C.; Balestro, F.; Wernsdorfer, W.; Ruben, M. Molecular spin qudits for quantum algorithms. *Chem. Soc. Rev.* **2018**, *47* (2), 501−513.
(8) Cornia, A.; Mannini, M.; Sainctavit, P.; Sessoli, R. Chemical strategies and characterization tools for the organization of single molecule magnets on surfaces. *Chem. Soc. Rev.* **2011**, *40* (6), 3076−3091.
(9) Chiesa, A.; Cugini, F.; Hussain, R.; Macaluso, E.; Allodi, G.; Garlatti, E.; Giansiracusa, M.; Goodwin, C. A. P.; Ortu, F.; Reta, D.; Skelton, J. M.; Guidi, T.; Santini, P.; Solzi, M.; De Renzi, R.; Mills, D. P.; Chilton, N. F.; Carretta, S. Understanding magnetic relaxation in single-ion magnets with high blocking temperature. *Phys. Rev. B* **2020**, *101* (17), 174402.
(10) Guo, F.-S.; Day, B. M.; Chen, Y.-C.; Tong, M.-L.; Mansikkamäki, A.; Layfield, R. A. Magnetic hysteresis up to 80 K in a dysprosium metallocene single-molecule magnet. *Science* **2018**, *362* (6421), 1400−1403.
(11) Ishikawa, N.; Sugita, M.; Ishikawa, T.; Koshihara, S.-y.; Kaizu, Y. Lanthanide double-decker complexes functioning as magnets at the single-molecular level. *J. Am. Chem. Soc.* **2003**, *125* (29), 8694−8695.
(12) Thiele, S.; Balestro, F.; Ballou, R.; Klyatskaya, S.; Ruben, M.; Wernsdorfer, W. Electrically driven nuclear spin resonance in single-molecule magnets. *Science* **2014**, *344* (6188), 1135−1138.
(13) Gould, C. A.; McClain, K. R.; Reta, D.; Kragskow, J. G. C.; Marchiori, D. A.; Lachman, E.; Choi, E.-S.; Analytis, J. G.; Britt, R. D.; Chilton, N. F.; Harvey, B. G.; Long, J. R. Ultrahard magnetism from mixed-valence dilanthanide complexes with metal-metal bonding. *Science* **2022**, *375* (6577), 198−202.
(14) Ungur, L.; Chibotaru, L. F. Strategies toward high-temperature lanthanide-based single-molecule magnets. *Inorg. Chem.* **2016**, *55* (20), 10043−10056.
(15) Mondal, K. C.; Sundt, A.; Lan, Y.; Kostakis, G. E.; Waldmann, O.; Ungur, L.; Chibotaru, L. F.; Anson, C. E.; Powell, A. K. Coexistence of Distinct Single-Ion and Exchange-Based Mechanisms for Blocking of Magnetization in a $Co^{II2}Dy^{III2}$ Single-Molecule Magnet. *Angew. Chem., Int. Ed.* **2012**, *51* (30), 7550−7554.
(16) Gu, L.; Wu, R. Origins of Slow Magnetic Relaxation in Single-Molecule Magnets. *Phys. Rev. Lett.* **2020**, *125* (11), 117203.
(17) Moreno-Pineda, E.; Taran, G.; Wernsdorfer, W.; Ruben, M. Quantum tunnelling of the magnetisation in single-molecule magnet isotopologue dimers. *Chem. Sci.* **2019**, *10* (19), 5138−5145.
(18) Graham, M. J.; Krzyaniak, M. D.; Wasielewski, M. R.; Freedman, D. E. Probing Nuclear Spin Effects on Electronic Spin Coherence via EPR Measurements of Vanadium (IV) Complexes. *Inorg. Chem.* **2017**, *56* (14), 8106−8113.
(19) Troiani, F.; Affronte, M. Molecular spins for quantum information technologies. *Chem. Soc. Rev.* **2011**, *40* (6), 3119−3129.
(20) Zadrozny, J. M.; Niklas, J.; Poluektov, O. G.; Freedman, D. E. Millisecond coherence time in a tunable molecular electronic spin qubit. *ACS Cent. Sci.* **2015**, *1* (9), 488−492.
(21) Atzori, M.; Tesi, L.; Morra, E.; Chiesa, M.; Sorace, L.; Sessoli, R. Room-temperature quantum coherence and rabi oscillations in vanadyl phthalocyanine: toward multifunctional molecular spin qubits. *J. Am. Chem. Soc.* **2016**, *138* (7), 2154−2157.
(22) Atzori, M.; Morra, E.; Tesi, L.; Albino, A.; Chiesa, M.; Sorace, L.; Sessoli, R. Quantum Coherence Times Enhancement in Vanadium(IV)-based Potential Molecular Qubits: the Key Role of the Vanadyl Moiety. *J. Am. Chem. Soc.* **2016**, *138* (35), 11234−11244.
(23) Zadrozny, J. M.; Niklas, J.; Poluektov, O. G.; Freedman, D. E. Multiple quantum coherences from hyperfine transitions in a vanadium (IV) complex. *J. Am. Chem. Soc.* **2014**, *136* (45), 15841−15844.
(24) Sun, Z.; Hendrickson, D. N.; Sun, Z.; Grant, C. M.; Castro, S. L.; Christou, G. Single-molecule magnets: Out-of-phase ac susceptibility signals from tetranuclear vanadium(III) complexes with an S = 3 ground state. *Chem. Commun.* **1998**, *2* (6), 721−722.
(25) Zhang, S.-Y.; Guo, W.-B.; Tang, Y.-Y.; Xu, J.-Q.; He, Z.-Z. Observation of Spin Relaxation in a Vanadate Chloride with Quasi-One-Dimensional Linear Chain. *Cryst. Growth Des.* **2019**, *19* (4), 2228−2234.
(26) Tidmarsh, I. S.; Batchelor, L. J.; Scales, E.; Laye, R. H.; Sorace, L.; Caneschi, A.; Schnack, J.; McInnes, E. J. L. Tri-, tetra- and octametallic vanadium(III) clusters from new, simple starting materials: interplay of exchange and anisotropy effects. *Dalton Trans.* **2009**, *43*, 9402−9409.
(27) Thakre, D.; Ali, S. R.; Mehta, S.; Alam, N.; Ibrahim, M.; Sarma, D.; Mondal, A.; De, M.; Banerjee, A. Polyoxovanadates with Ethylidene-Pyridine Functionalized Bisphosphonate Ligands: Synthesis, Structure, Spectroscopic Characterization, Magnetic, and Antibacterial Studies. *Cryst. Growth Des.* **2021**, *21* (8), 4285−4298.
(28) Vannathan, A. A.; Thakre, D.; Ali, S. R.; De, M.; Banerjee, A.; Mal, S. S. Investigations into the supercapacitor activity of bisphosphonate-polyoxovanadate compounds. *J. Solid State Chem.* **2021**, *304*, 122566.
(29) Tesi, L.; Lucaccini, E.; Cimatti, I.; Perfetti, M.; Mannini, M.; Atzori, M.; Morra, E.; Chiesa, M.; Caneschi, A.; Sorace, L.; et al. Quantum coherence in a processable vanadyl complex: New tools for the search of molecular spin qubits. *Chem. Sci.* **2016**, *7* (3), 2074−2083.

https://doi.org/10.1021/acs.cgd.2c00754
Cryst. Growth Des. 2022, 22, 5666−5679

(30) El Moll, H.; Zhu, W.; Oldfield, E.; Rodriguez-Albelo, L. M.; Mialane, P.; Marrot, J.; Vila, N.; Mbomekallé, I. M.; Rivière, E.; Duboc, C.; et al. Polyoxometalates functionalized by bisphosphonate ligands: Synthesis, structural, magnetic, and spectroscopic characterizations and activity on tumor cell lines. *Inorg. Chem.* **2012**, *51* (14), 7921−7931.
(31) Livage, J. Synthesis of polyoxovanadates via "chimie douce. *Coord. Chem. Rev.* **1998**, *178*−*180*, 999−1018.
(32) Correia, I.; Pessoa, J. C.; Duarte, M. T.; da Piedade, M. F. M.; Jackush, T.; Kiss, T.; Castro, M. M. C. A.; Geraldes, C. F. G. C.; Avecilla, F. Vanadium(IV and V) Complexes of Schiff Bases and Reduced Schiff Bases Derived from the Reaction of Aromatic o-Hydroxyaldehydes and Diamines: Synthesis, Characterisation and Solution Studies. *Eur. J. Inorg. Chem.* **2005**, *2005* (4), 732−744.
(33) Tsaramyrsi, M.; Kaliva, M.; Salifoglou, A.; Raptopoulou, C.; Terzis, A.; Tangoulis, V.; Giapintzakis, J. Vanadium (IV)− citrate complex interconversions in aqueous solutions. A pH-dependent synthetic, structural, spectroscopic, and magnetic study. *Inorg. Chem.* **2001**, *40* (23), 5772−5779.
(34) Nuber, B.; Weiss, J. Aqua(dipicolinato)(hydroxylamido-N,O)-oxovanadium. *Acta Cryst. B* **1981**, *37* (4), 947−948.
(35) Pinsky, M.; Avnir, D. Continuous Symmetry Measures. 5. The Classical Polyhedra. *Inorg. Chem.* **1998**, *37* (21), 5575−5582.
(36) Zabrodsky, H.; Peleg, S.; Avnir, D. Symmetry as a continuous feature. *IEEE Trans. Pattern Anal. Mach. Intell.* **1995**, *17* (12), 1154−1166.
(37) Singh, S. K.; Eng, J.; Atanasov, M.; Neese, F. Covalency and chemical bonding in transition metal complexes: An ab initio based ligand field perspective. *Coord. Chem. Rev.* **2017**, *344*, 2−25.
(38) Chilkuri, V. G.; DeBeer, S.; Neese, F. Ligand Field Theory and Angular Overlap Model Based Analysis of the Electronic Structure of Homovalent Iron−Sulfur Dimers. *Inorg. Chem.* **2020**, *59* (2), 984−995.
(39) Dragancea, D.; Talmaci, N.; Shova, S.; Novitchi, G.; Darvasiova, D.; Rapta, P.; Breza, M.; Galanski, M.; Kožíšek, J.; Martins, N. M.; et al. Vanadium (V) complexes with substituted 1, 5-bis (2-hydroxybenzaldehyde) carbohydrazones and their use as catalyst precursors in oxidation of cyclohexane. *Inorg. Chem.* **2016**, *55* (18), 9187−9203.
(40) Wen, D.; Zhou, J.; Zou, H.-H. A series of new oxo-vanadium (IV) complexes with octahedral coordinated vanadium centers. *J. Coord. Chem.* **2019**, *72* (5−7), 1064−1074.
(41) Mehio, N.; Ivanov, A. S.; Ladshaw, A. P.; Dai, S.; Bryantsev, V. S. Theoretical study of oxovanadium (IV) complexation with formamidoximate: implications for the design of uranyl-selective adsorbents. *Ind. Eng. Chem. Res.* **2016**, *55* (15), 4231−4240.
(42) Smith, K. I.; Borer, L. L.; Olmstead, M. M. Vanadium (IV) and vanadium (V) complexes of salicyladimine ligands. *Inorg. Chem.* **2003**, *42* (23), 7410−7415.
(43) Klich, P. R.; Daniher, A. T.; Challen, P. R.; McConville, D. B.; Youngs, W. J. Vanadium (IV) complexes with mixed O, S donor ligands. Syntheses, structures, and properties of the anions tris (2-mercapto-4-methylphenolato) vanadate (IV) and bis (2-mercapto-phenolato) oxovanadate (IV). *Inorg. Chem.* **1996**, *35* (2), 347−356.
(44) Glendening, E. D.; Landis, C. R.; Weinhold, F. NBO 6.0: Natural bond orbital analysis program. *J. Comput. Chem.* **2013**, *34* (16), 1429−1437.
(45) Sheikhshoaie, I.; Ebrahimipour, S. Y.; Crochet, A.; Fromm, K. M. Synthesis, X-ray structure and DFT calculation of oxido-vanadium (V) complex with a tridentate Schiff base ligand. *Res. Chem. Intermed.* **2015**, *41* (4), 1881−1891.
(46) Smith, T. S., II; LoBrutto, R.; Pecoraro, V. L. Paramagnetic spectroscopy of vanadyl complexes and its applications to biological systems. *Coord. Chem. Rev.* **2002**, *228*, 1−18.
(47) Ban, R.; Liang, Y.; Ma, P.; Zhang, D.; Niu, J.; Wang, J. Synthesis, crystal structure, characterization and magnetic property of a new organophosphonate-based polyoxovanadate. *Inorg. Chem. Commun.* **2016**, *71*, 65−67.
(48) Ziegenbalg, S.; Hornig, D.; Görls, H.; Plass, W. Cobalt(II)-Based Single-Ion Magnets with Distorted Pseudotetrahedral [N2O2] Coordination: Experimental and Theoretical Investigations. *Inorg. Chem.* **2016**, *55* (8), 4047−4058.
(49) Meijer, P. H. A group theoretical proof of Kramers' theorem. *Physica* **1960**, *26* (1), 61−65.
(50) Wang, J.; Wang, H.; Ma, Y.; Tang, J.; Li, L.; Wang, Q.; Zhao, B.; Cheng, P.; Ma, J. Enhancing magnetic behaviors of dysprosium single-molecule magnets from crystal field perturbation by deprotonating Schiff-Base ligand. *Cryst. Growth Des.* **2019**, *19* (6), 3365−3371.
(51) Nehrkorn, J.; Valuev, I. A.; Kiskin, M. A.; Bogomyakov, A. S.; Suturina, E. A.; Sheveleva, A. M.; Ovcharenko, V. I.; Holldack, K.; Herrmann, C.; Fedin, M. V.; et al. Easy-plane to easy-axis anisotropy switching in a Co(II) single-ion magnet triggered by the diamagnetic lattice. *J. Mater. Chem. C* **2021**, *9* (30), 9446−9452.
(52) Fackler, J. P., Jr; Levy, J. D.; Smith, J. A. Electron paramagnetic resonance spectra of copper (II) and oxovanadium (IV) complexes oriented in nematic glasses from liquid crystal solvent. *J. Am. Chem. Soc.* **1972**, *94* (7), 2436−2445.
(53) Rechkemmer, Y.; Breitgoff, F. D.; van der Meer, M.; Atanasov, M.; Hakl, M.; Orlita, M.; Neugebauer, P.; Neese, F.; Sarkar, B.; van Slageren, J. A four-coordinate cobalt(II) single-ion magnet with coercivity and a very high energy barrier. *Nat. Commun.* **2016**, *7* (1), 10467.
(54) Stinghen, D.; Atzori, M.; Fernandes, C. M.; Ribeiro, R. R.; De Sá, E. L.; Back, D. F.; Giese, S. O.; Hughes, D. L.; Nunes, G. G.; Morra, E.; et al. A Rare Example of Four-Coordinate Nonoxido Vanadium (IV) Alkoxide in the Solid State: Structure, Spectroscopy, and Magnetization Dynamics. *Inorg. Chem.* **2018**, *57* (18), 11393−11403.
(55) Krzystek, J.; Ozarowski, A.; Telser, J.; Crans, D. C. High-frequency and-field electron paramagnetic resonance of vanadium (IV, III, and II) complexes. *Coord. Chem. Rev.* **2015**, *301*−*302*, 123−133.
(56) Rowlands, C. C.; Murphy, D. M.. EPR Spectroscopy, Theory. In *Encyclopedia of Spectroscopy and Spectrometry*, 3rd ed.; Lindon, J. C., Tranter, G. E., Koppenaal, D. W., Eds.; Elsevier Ltd., 2017; pp 517−526.
(57) Devi, R. B.; Devi, S. P.; Singh, R. H. Synthesis, characterization and DNA interaction study of a new oxovanadium (IV) complex containing acetylacetone and Dicyandiamide as ligands. *Spectrosc. Lett.* **2012**, *45* (2), 93−103.
(58) Mustafi, D.; Galtseva, E.; Krzystek, J.; Brunel, L.-C.; Makinen, M. High-Frequency Electron Paramagnetic Resonance Studies of VO^{2+} in Low-Temperature Glasses. *J. Phys. Chem. A* **1999**, *103* (51), 11279−11286.
(59) Smith, T. S., II; LoBrutto, R.; Pecoraro, V. L. Paramagnetic spectroscopy of vanadyl complexes and its applications to biological systems. *Coord. Chem. Rev.* **2002**, *228* (1), 1−18.
(60) Sheldrick, G. A Short History of ShelX. *Acta crystallogr., Sect. A: Found. crystallogr.* **2008**, *64* (1), 112−122.
(61) Sheldrick, G. M.et al.*SADABS, Program for Empirical Absorption Correction of Area Detector Data*; University of Göttingen: Göttingen, Germany1996.
(62) Frisch, M.; Trucks, G. W.; Schlegel, H. B.; Scuseria, G. E.; Robb, M. A.; Cheeseman, J. R.; Scalmani, G.; Barone, V.; Petersson, G. A.; Nakatsuji, H. *Gaussian 16*, rev. A.03.; Gaussian, Inc.: Wallingford, CT. 2016.
(63) Grimme, S.; Ehrlich, S.; Goerigk, L. Effect of the damping function in dispersion corrected density functional theory. *J. Comput. Chem.* **2011**, *32* (7), 1456−1465.
(64) Weigend, F.; Ahlrichs, R. Balanced basis sets of split valence, triple zeta valence and quadruple zeta valence quality for H to Rn: Design and assessment of accuracy. *Phys. Chem. Chem. Phys.* **2005**, *7* (18), 3297−3305.
(65) Allouche, A. R. Gabedit—A graphical user interface for computational chemistry softwares. *J. Comput. Chem.* **2011**, *32* (1), 174−182.

https://doi.org/10.1021/acs.cgd.2c00754
Cryst. Growth Des. 2022, 22, 5666−5679

(66) Grimme, S.; Antony, J.; Ehrlich, S.; Krieg, H. A consistent and accurate ab initio parametrization of density functional dispersion correction (DFT-D) for the 94 elements H-Pu. *J. Chem. Phys.* **2010**, *132* (15), 154104.
(67) Weigend, F. Accurate Coulomb-fitting basis sets for H to Rn. *Phys. chem. chem. phys.* **2006**, *8* (9), 1057−1065.
(68) Neese, F. Software Update: The ORCA program system-Version 5.0. *WIREs Comput. Mol. Sci.* **2022**, No. e1606.
(69) Stoll, S.; Schweiger, A. EasySpin, a comprehensive software package for spectral simulation and analysis in EPR. *J. Magn. Reson.* **2006**, *178* (1), 42−55.

https://doi.org/10.1021/acs.cgd.2c00754
Cryst. Growth Des. 2022, 22, 5666−5679